Available online at www.sciencedirect.com
SCIENCE DIRECT®
International Journal of Heat and Mass Transfer 48 (2005) 4867–4886
International Journal of HEAT and MASS TRANSFER
www.elsevier.com/locate/ijhmt

Boiling heat transfer in rectangular microchannels with reentrant cavities

Ali Koşar, Chih-Jung Kuo, Yoav Peles *

Department of Mechanical, Aerospace and Nuclear Engineering, Rensselaer Polytechnic Institute, Troy, NY 12180, United States

Received 3 December 2004; received in revised form 26 April 2005
Available online 18 August 2005

Abstract

This paper investigates flow boiling of water in microchannels with a hydraulic diameter of 227 μm possessing 7.5 μm wide reentrant cavities on the sidewalls. Average two-phase heat transfer coefficients and CHF conditions have been obtained over a range of effective heat fluxes (28–445 W/cm^2) and mass velocities (41–302 kg/m^2 s). High Boiling number and Reynolds number have been found to promote convective boiling, while Nucleate Boiling dominated at low Reynolds number and Boiling number. A criterion for the transition between nucleate and convective boiling has been provided. Existing correlations did not provide satisfactory agreement with the heat transfer coefficient but did predict CHF conditions well.

Keywords: Microchannels; Boiling; Reentrant cavity; Enhanced

1. Introduction

The last few years have witnessed a surge in research activities on boiling in microchannels [1–7]. This research thrust has provided immense knowledge and insight into heat transfer and fluid flow mechanisms governing boiling in microchannels, and has resulted in heat transfer correlations and flow pattern identifications. Although there remain many challenges within the current generation of microchannels, the state-of-the-art knowledge in the field is such that the heat transfer community is ready to take new challenges and advance the development of more sophisticated second-generation microchannels.

Perhaps the most significant advances in enhanced heat transfer technology for conventional scale channels have been made in special surface geometries that promote high-performance nucleate boiling. These special surfaces can significantly reduce the boiling inception superheat (ΔT_{sat}), substantially increase the heat transfer coefficient (h) and the CHF (critical heat flux) conditions. Enhanced heat transfer surfaces are known to improve heat transfer coefficients by a factor of four at low to medium vapor quality [8–16], produce a twofold increase in CHF values [17,18], and reduce incipient superheat by 80–90% [18,19].

On roughened surfaces boiling enhancement occurs due to the increased number of active cavities that trap vapor and provide more and larger sites for bubble growth. However, under prolonged boiling, the effect of surface roughness generally diminishes, due to a phenomenon known as "aging". Cavities formed by

* Corresponding author. Tel.: +1 518 276 2886; fax: +1 518 276 2623.
E-mail address: pelesy@rpi.edu (Y. Peles).

0017-9310/$ - see front matter © 2005 Elsevier Ltd. All rights reserved.
doi:10.1016/j.ijheatmasstransfer.2005.06.003

Nomenclature

A'	parameter in Correlation 11
C'	parameter in Correlation 11
A_f	fin surface area, m^2
A_s	surface area, m^2
A_p	planform area, m^2
A_t	total heat transfer area, m^2
Bo	Boiling number, $\frac{q''_{ch}}{Gh_{FG}}$
C	constant
Co	convection number, $\left(\frac{\rho_G}{\rho_L}\right)^{0.5}\left(\frac{1-x}{x}\right)^{0.8}$
const	constant
d_h	hydraulic diameter, m
E	parameter in Correlation 7
f	friction factor
F	correction factor, $\frac{1-1.883\beta+3.767\beta^2-5.814\beta^3+5.361\beta^4-2.0\beta^5}{1-2.042\beta+3.085\beta^2-2.477\beta^3+1.058\beta^4-0.186\beta^5}$
F_{B1}, F_{B2}, F_{B3}, F_{B4}	parameters in Correlation 11
F_{nb}, F_{tp}	parameters in Correlation 8
G	mass flux, kg/m^2 s
h	heat transfer coefficient, W/m^2 K
$\bar{h}$	average heat transfer coefficient, W/m^2 K
h_{FG}	latent heat of vaporization, kJ/kg
H	channel height, m
I	electrical current, A
k	thermal conductivity, W/m K
K	parameter in Correlation 12
k_I	dimensionless parameter, $\left(\frac{q''}{Gh_{FG}}\right)^2\frac{\rho_L}{\rho_G}$
L	microchannel length, m
m	defined in Eq. (7)
M	number of data points
M_W	molecular weight, kg/kmol
MAE	mean absolute error
n	constant
N	number of microchannels
p	pressure, kPa
P	power, W
P_r	reduced pressure, p/p_{cr}
Pr	Prandtl number
q''	heat flux, W/cm^2
$\dot{Q}$	volumetric flow rate, ml/min
S	parameter in Correlation 7
R	electrical resistance, Ω
Re	Reynolds number, $\frac{Gd_h}{\mu}$
t	thickness between the heater and microchannel base, m
T	temperature, °C
$\overline{T}$	average temperature, °C
ΔT	temperature difference, °C
U	quantity under consideration
V	voltage, V
W	microchannel width, m
W_b	fin width, m
We	Weber number, $\frac{G^2 d_h}{\rho_L \sigma}$
x	mass quality
X	parameter in Correlation 12
X_{vt}	Lockhardt–Martinelli parameter

Greek symbols

β	aspect ratio, $\frac{w}{H}$
η	efficiency
μ	viscosity, kg/ms
ρ	density, m^3/s
σ	surface tension, N/m
υ	specific volume, m^3/kg
ϕ_F	two-phase frictional multiplier

Subscripts

amb	ambient
CHF	critical heat flux
cr	critical
e	exit
eff	effective
exp	experimental
f	fin
F	fluid
G	gas
i	inlet
LO	liquid only
nb	nucleate boiling
o	overall
pool	pool boiling
s	surface
sat	saturation
se	surface at the exit
si	surface at the inlet
sp	single-phase
sub	subcooled flow
theo	theoretical
tp	two-phase

roughening the surface are often not stable vapor traps and slowly degas with time, leaving no vapor to sustain the nucleation process. For this reason there have been very few studies on that topic for nearly 35 years following the early work by Jakob and Fritz in 1931 [20].

To overcome the "aging" effect, extensive studies in the late fifties and early sixties were made to understand the characteristics of nucleation sites necessary to form stable vapor traps. Consequently, various porous surfaces, containing reentrant type cavity geometries, were developed and patented that were shown to be stable

for prolonged enhanced boiling heat transfer. A comprehensive review of such geometries has been given by Webb [21,22]. Griffith and Wallis [23] showed that cavity geometry for naturally occurring surface pits and scratches is important in two respects: the mouth diameter determines the superheat needed to initiate boiling, and its shape determines its stability once boiling has begun.

Benjamin and Westwater [24] were the first to construct reentrant cavities and demonstrated their superior performance as a vapor trap. Yatabe and Westwater [25] showed that the interior shape of a reentrant cavity is not important. Gottzmann et al. [26] theorized that in reentrant cavities all vaporization occurs within the porous matrix, and the high performance is the result of two factors: (1) The porous structure entraps large radius vapor–liquid interfaces, compared to the very small nuclei in naturally occurring pits and scratches, which considerably reduces the theoretical superheat required for nucleation. (2) The porous structure provides a much larger surface area for thin film or microlayer evaporation than exists with flat surfaces.

From the aforementioned discussion it is clear that enormous advantages are ingrained in reentrant cavities for enhanced boiling heat transfer in conventional scale channels. However, reentrant cavities in microchannels have not been studied before. This study aims at providing evidence on the enhanced heat transfer performance of reentrant cavities formed on the surface of microchannels (Fig. 1) for the very first time. Additionally, results have been compared with both existing microchannel boiling data as well as large-scale data. Existing correlations have been assessed in terms of their ability to predict heat transfer coefficients and CHF condition. Finally, a modified correlation based on the experimental data obtained in the current experiments is proposed for boiling flows in microchannels with reentrant cavities.

2. Experimental device, apparatus and procedure

2.1. Microchannel device

Fig. 1 shows a CAD image of the microchannel device consisting of five 1 cm long, 200 μm wide and 264 μm deep, parallel microchannels, spaced 200 μm apart. On each channel wall the array of 100 interconnected reentrant cavities (Fig. 1b and c) are 100 μm apart. An acute angle connects the 7.5 μm mouth to the reentrant body (Fig. 1e) and ensures its stability [22]. In order to minimize ambient heat losses an air gap is formed on the two ends of the side walls (Fig. 1), and an inlet and exit plenum are etched on the thin silicon substrate (~150 μm). Pyrex substrate seals the microchannels device from the top, and allows flow visualization. Five 20-μm wide orifices are installed (Fig. 1d) at the entrance of each channel to suppress flow instabilities. Flow distributive pillars have been employed to provide homogeneous distribution of flow in the inlet (Fig. 1f). They are arranged in 2 columns of 12 circular pillars having a diameter of 100 μm. The transverse pitch between the pillars is 150 μm and equal to the longitudinal pitch. A heater (Fig. 2) is deposited on the back side to deliver the heating power, and also serves as a thermistor for temperature measurements.

2.2. Fabrication of the MEMS device

The MEMS (microelectromechanical sysytems) device is micromachined on a polished double-sided n-type ⟨1 0 0⟩ single crystal silicon wafer employing techniques adapted from IC manufacturing. It is equipped with pressure ports at the inlet and the exit to obtain accurate static pressure measurements. A schematic representation of the primary steps in the process flow is displayed in Fig. 3.

A 1.5 μm thick high quality oxide is deposited on both sides of the silicon wafer to shield the bare wafer surface during processing. The heater and the via's are formed on the backside of the wafer by CVC sputtering. A 70 Å thick layer of titanium is initially deposited to enhance adhesion characteristics and is followed by sputtering a 1 μm thick layer of aluminum containing 1% silicon and 4% copper. Subsequent photolithography and concomitant wet bench processing create the heater on the backside of the wafer. A 1 μm thick PECVD (plasma enhanced chemical vapor deposition) oxide is deposited to protect the heater during further processing.

Next, the microchannels are formed on the top side of the wafer. The wafer is taken through a photolithography step and an oxide removal process (reactive ion etching) to mask certain areas on the wafer, which are not to be etched during the DRIE (deep reactive ion etching) process. The wafer is consequently etched in a DRIE process and silicon is removed from places not protected by the photoresist/oxide mask. This creates an array of microchannels along with the reentrant cavities. The DRIE process forms deep vertical trenches on the silicon wafer with a characteristic scalloped sidewall possessing a peak-to-peak roughness of ~0.3 μm. A profilometer and SEM are employed to measure and record various dimensions of the device.

The wafer is flipped and the backside is then processed to create an inlet, outlet, side air gap, and pressure port taps for the transducers. A photolithography followed by a BOE (6:1) oxide removal process is carried out to create a pattern mask. The wafer is then etched-through in a DRIE process to create the fluidic ports. Thereafter, electrical contacts/pads are opened on the backside of the wafer by performing another round of photolithography and RIE processing. Finally, the

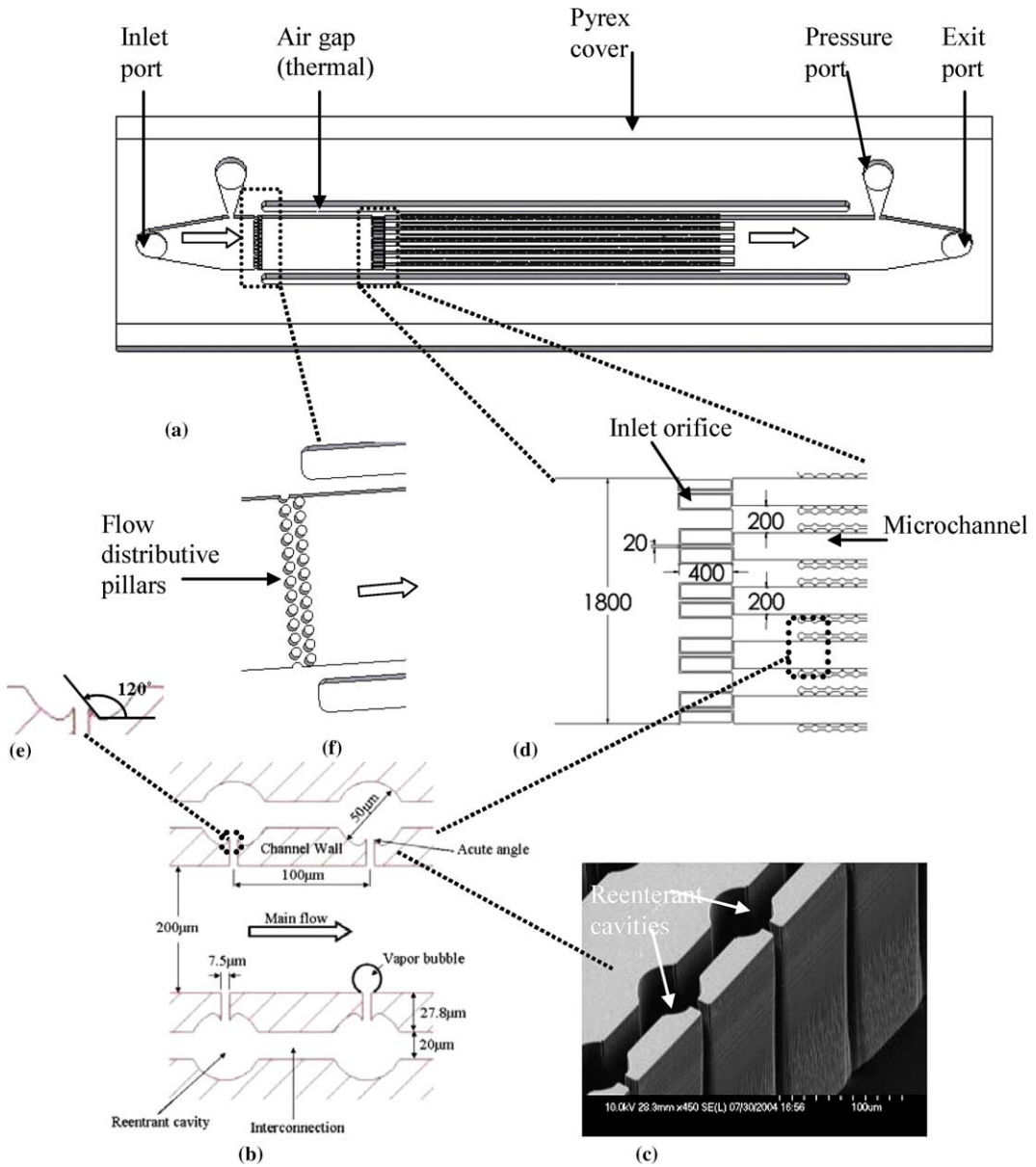

Fig. 1. (a) CAD model of the microchannel device, (b) dimensions of reentrant cavities, (c) SEM image of reentrant cavities, (d) geometry of the inlet region, (e) geometry of the reentrant cavity, and (f) flow distributive pillars.

processed wafer is stripped of any remaining resist or oxide layers and anodically bonded to a 1 mm thick polished Pyrex (glass) wafer to form a sealed device. After successful completion of the bonding process, the processed stack is die-sawed to separate the devices from the parent wafer.

2.3. Experimental apparatus

In Fig. 4b, a schematic of the experimental setup is shown. It consists of a refrigeration loop including a pump, filter, flowmeters (rotameters), packaging module, and the MEMS device. While the working fluid circulates in the loop, resistance, pressure, and flow measurements are made at various locations. The MEMS device is packaged by sandwiching it between two plates, as shown in Fig. 4a. The fluidic seals are forged using miniature "o-rings", while the external electrical connections to the heater are achieved from beneath through spring-loaded pins, which connect the heater to electrical pads residing away from the main microchannels' body.

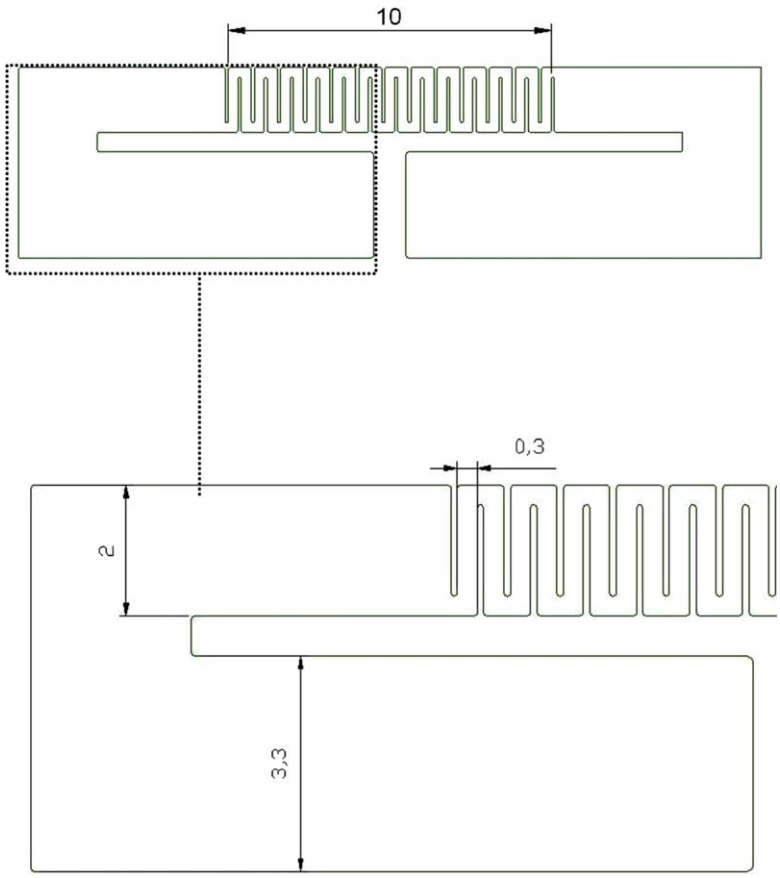

Fig. 2. CAD model of the heater (dimensions in mm).

The electrical power is supplied to the device with an INSTEK programmable power supply, which enables the measurement of electrical current and voltage. A HNP Mikrosysteme microannular gear pump capable of generating flowrates from 0.3 to 18 ml/min is used to propel the liquid from a reservoir through the MEMS device at various flow rates. A Welch vacuum pump is employed to evacuate air in the system prior to any liquid circulation. Flow data is measured via pressure transducers and an Omega F-111 flow meter, and is acquired together with the voltage and current data using an IBM PC. The microchannel heat sink is continuously scanned using a microscope and flow images are recorded via a Vision Research Phantom V-4 series high-speed camera, which has the ability to capture frames with a rate up to 90,000 frames/s, a maximum resolution of 512×512 pixels, and a minimum exposure time of 2 μs.

2.4. Experimental procedure

Prior to the experiments, an identical device to the one tested without a flow restrictor has been hydrodynamically tested to obtain pressure drops across microchannels. Pressure drops measurements of the orificeless device have yielded 0.4, 0.8, 1.7, and 3.0 kPa for $G = 41$, 83, 166, 302 kg/m^2 s, respectively.

The flow rate is fixed at the desired value, and experiments are conducted after steady flow conditions are reached under atmospheric exit pressure. The flow rate is read from the Omega FL-111 flowmeter, while the pressure difference is recorded through a LabView® interface to a spreadsheet file. All experiments are performed under ambient room temperature. DI water is utilized as the working fluid, and enters to the microchannel device at room temperature. First, the electrical resistance of the device is measured at room temperature. Thereafter, voltage is applied in 1 V increments across the heater, and the current/voltage data is recorded once steady state has been reached. Flow visualization through the high-speed camera and microscope compliments the measured data. The procedure is repeated for different flow rates.

In order to estimate heat losses, electrical power is applied to the test section after evacuating water from

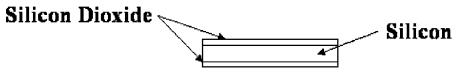

(a) Silicon dioxide deposition on both side of the wafer.

(b) Al heater deposition on the back side of the wafer.

(c) Silicon dioxide etch to open etch holes.

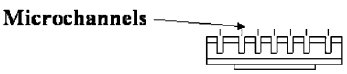

(d) Silicon deep etch on the top to create microchannels.

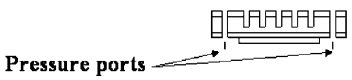

(e) Silicon deep etch on the back side of the wafer to create inlet, outlet, air gaps, and pressure ports.

(f) Top side silicon dioxide stripping.

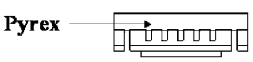

(g) Silicon to Pyrex anodic bonding.

Fig. 3. Process flow of the microfluidic device.

the test loop. Once the temperature of the test section becomes steady, the temperature difference of the ambience and test section is recorded with the corresponding power. The plot of power versus temperature difference is used to calculate the heat loss associated with each of experimental data point. The corresponding values have been used in subsequent analysis of the data reduction.

3. Data reduction

The data obtained from the voltage, current and pressure measurements are used to derive the average single- and two-phase temperatures, heat transfer coefficients, and CHF conditions. The electrical input power and resistance can be found as, respectively,

$$P = V \times I, \tag{1}$$

and

$$R = V/I. \tag{2}$$

Prior to the experimental runs, the device is placed in a well insulated and temperature controlled oven. As the temperature of the oven is increased, the resistance across the device is recorded, so that the heater electrical resistance-temperature calibration curve is generated. The temperature resistance curve of the aluminum heater is linear and therefore, the electrical resistance is an accurate measure of the average temperature. The following curve is used in subsequent analysis to adjust the temperature measurement obtained during the experimental tests:

$$\overline{T} = 394.2\left(\frac{R}{6.63} - 1\right). \tag{3}$$

The surface temperature at the base of the microchannels is then calculated using the average surface temperature of the heater as

$$\overline{T} = \overline{T}_{\text{heater}} - \frac{q''_{\text{eff}} t}{k_s}, \tag{4}$$

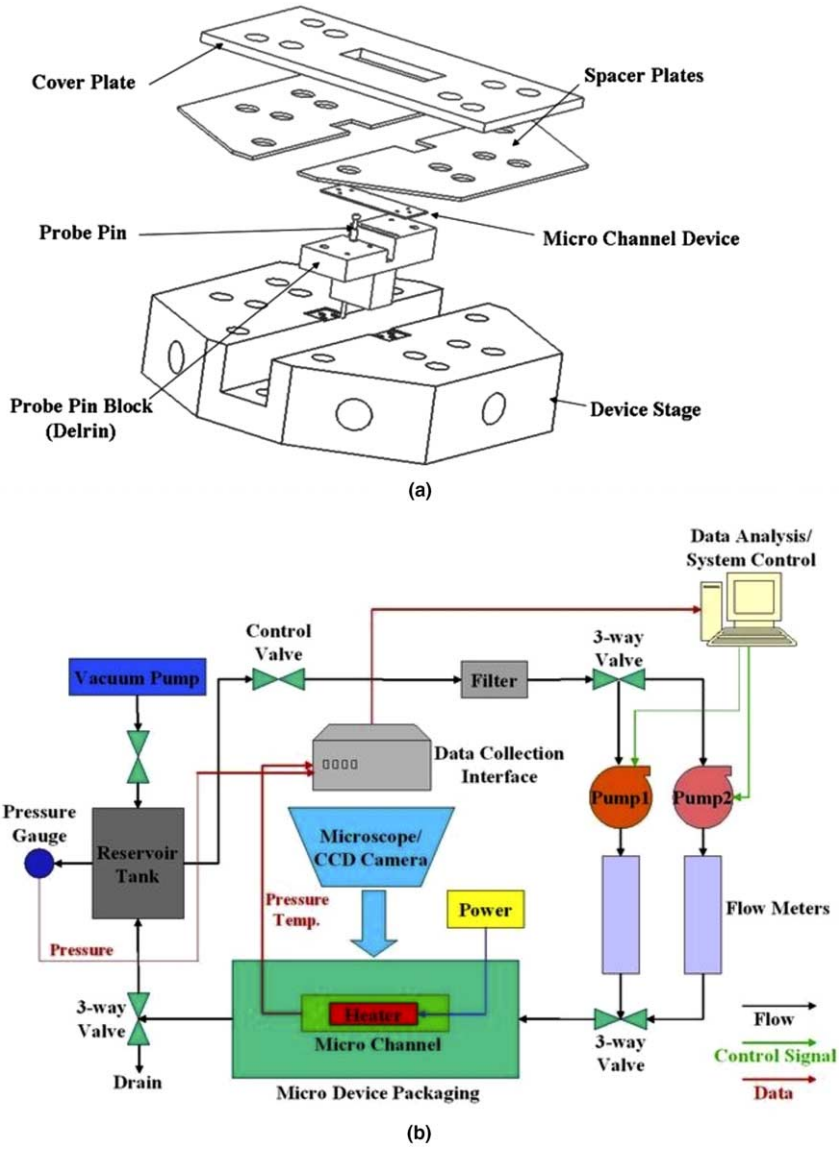

Fig. 4. (a) Device package and (b) experimental setup.

where

$$q''_{\text{eff}} = \frac{P}{A_{\text{p}}}.$$

3.1. Single phase heat transfer

The exit single-phase fluid temperature is found by calorimetric balance, and the average fluid temperature is expressed as

$$\overline{T}_{\text{F}} = \frac{T_{\text{i}} + T_{\text{e}}}{2}. \tag{5}$$

The power input is related to the average single-phase heat transfer coefficient in terms of the average surface and fluid temperatures as (assuming adiabatic fin tip):

$$P = \eta_{\text{o}} A_{\text{t}} \bar{h} (\overline{T} - \overline{T}_{\text{F}}), \tag{6}$$

where η_{o} is the overall efficiency of the microchannels configuration and is expressed as

$$\eta_{\text{o}} = \frac{N\eta_{\text{f}} A_{\text{f}} + (A_{\text{t}} - NA_{\text{f}})}{A_{\text{t}}}, \tag{7}$$

where

$$\eta_f = \frac{\tanh(mH)}{mH},$$
$$m = \sqrt{\frac{\bar{h}2(L+W)}{k_s WL}}, \quad (8)$$
$$A_f = 2HL.$$

Eqs. (6)–(8) can be solved for $\bar{h}$ with an iterative scheme.

3.2. Boiling heat transfer

Under boiling conditions, the microchannels are divided into two length regions: single-phase (L_{sp}), and two-phase (L_{tp}). L_{tp} and L_{sp} are obtained by flow visualization. The single-phase length L_{sp} was defined as the distance between the inlet of microchannels and the location of first active nucleation sites detected in the reentrant cavities of microchannels, while the two-phase length L_{tp} is the difference between the microchannel length and the single-phase length. Using fin analysis on a single microchannel (Fig. 5), the average two-phase heat transfer coefficient, $\bar{h}_{tp}$, *can* be expressed as follows:

$$\bar{h}_{tp}(\overline{T}_{tp} - T_{sat})(W + A_f\eta_f)L = q''(W + A_f\eta_f)L = \frac{P(W + W_b)L}{A_p}. \quad (9)$$

The inlet and the exit surface temperatures are given as

$$T_{si,sp} = T_i + \frac{P}{\bar{h}A_s}, \quad (10)$$

$$T_{se,sp} = T_{sat} + \frac{P}{\bar{h}A_s}. \quad (11)$$

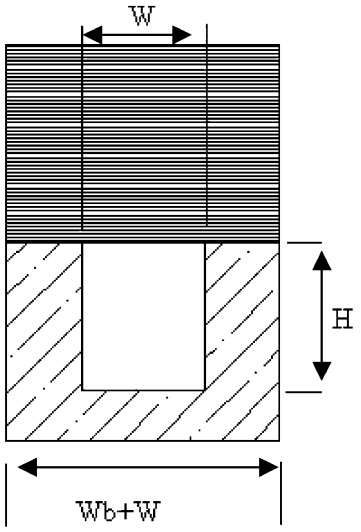

Fig. 5. Cross-section of a single microchannel.

Table 1
Uncertainties in variables used in uncertainty analysis

Uncertainty	Error
Flow rate, Q (for each reading)	1.0%
Voltage supplied by power source, V	0.5%
Current supplied by power source, I	0.5%
Ambient temperature, T_{amb}	0.1 °C
Electrical power, P	0.7%
Electrical resistance, R	0.7%
Average temperature, $\overline{T}$	1.0 °C
Two-phase heat transfer coefficient, $\bar{h}_{tp}$	9.0%

The average temperature in the single-phase region is the mean value of the above surface temperatures:

$$\overline{T}_{sp} = \frac{T_{si,sp} + T_{se,sp}}{2}. \quad (12)$$

With $\overline{T}_{sp}$, L_{sp}, and L_{sp} known $\overline{T}_{tp}$ is obtained using the weighted average method in terms of the single-phase and average wall temperatures:

$$\overline{T}_{tp} = \frac{\overline{T}L - \overline{T}_{sp}L_{sp}}{L_{tp}}. \quad (13)$$

Finally, the exit quality can be calculated with the known mass flow rate and net power supplied to the device as

$$x_e = \frac{P - \dot{m}c_p(T_{sat} - T_i)}{\dot{m}h_{FG}}. \quad (14)$$

Mean absolute error is used to compare the experimental results with various correlations according to the following expression:

$$MAE = \frac{1}{M}\sum_{i=1}^{M}\frac{|U_{exp} - U_{theoretical}|}{U_{exp}} \times 100\%. \quad (15)$$

3.3. Uncertainty analysis

The uncertainties of the measured values, given in Table 1, are obtained from the manufacturer's specification sheets, while the uncertainties of the derived parameters are calculated using the method developed by Kline and McClintock [27].

4. Results and discussion

4.1. Boiling curve

Fig. 6 shows the average surface temperature as a function of the heat flux at different mass velocities. As expected, during single-phase flow the curves follow the same slope for all mass velocities. The abrupt change in the slope at temperatures in the vicinity of 100 °C signifies the transition from single-phase to boiling flow. As

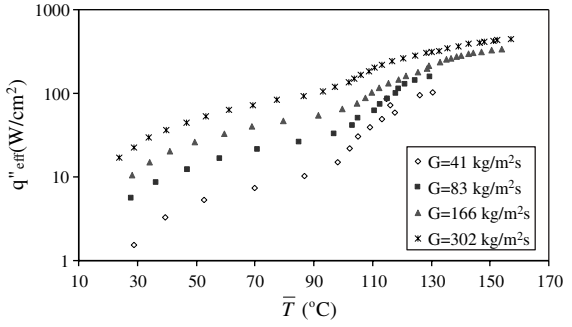

Fig. 6. q''_{eff} versus $\overline{T}$ profile.

the heat flux is further increased above a certain value the surface temperature abruptly surges with a meager rise of heat flux, indicating the emergence of critical heat flux (CHF) conditions, which is verified by flow visualizations of dry spots at the channel exit region.

4.2. Two-phase heat transfer coefficient

Fig. 7 shows two-phase heat transfer coefficient as a function of heat flux. The data for all mass velocities except for $G = 302$ kg/m^2 s shows very weak dependence on the mass velocity for $q'' = 41$–49 W/cm^2. For $G = 41$ kg/m^2 s the two-phase heat transfer coefficient drops sharply at $q'' = 50$ W/cm^2 indicating CHF conditions as a result of the complete dry-out ($x_e \sim 1$). The heat transfer coefficients for $G = 83$ kg/m^2 s and $G = 166$ kg/m^2 s appear to follow the same trend qualitatively as well as quantitatively for a much broader range (q'' from 41 to 71 W/cm^2). For $q'' > 80$ W/cm^2, heat transfer coefficient starts to decrease sharply with heat flux for $G = 83$ kg/m^2 s because of the impending CHF condition. The heat transfer coefficient for $G = 166$ kg/m^2 s at higher heat fluxes ($q'' > 80$ W/cm^2) declines with heat flux. For $G = 302$ kg/m^2 s, heat transfer coefficient monotonically decreases throughout the boiling flow starting from the onset of nucleate boiling to CHF conditions.

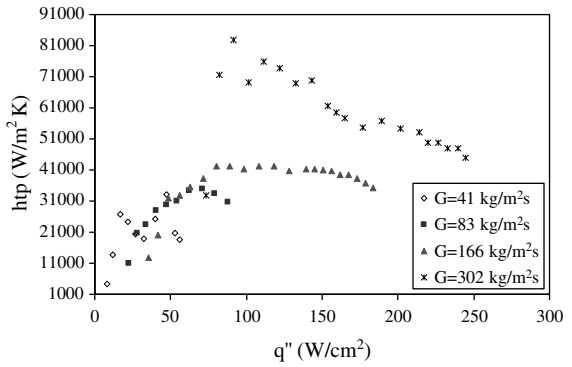

Fig. 7. $\bar{h}_{\text{tp}}$ versus q'' profile.

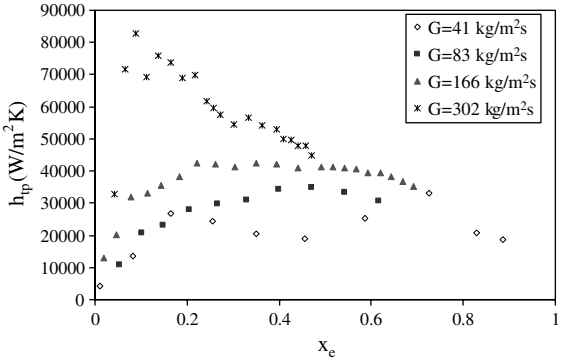

Fig. 8. $\bar{h}_{\text{tp}}$ versus x_e profile.

Fig. 8 shows the variation of two-phase heat transfer coefficient with exit quality for different mass velocities. For $G = 41$ kg/m^2 s, relatively large fluctuations in h_{tp} have been recorded. This is attributed to the oscillatory flow pattern observed in this low mass velocity during flow visualizations, which continuously shifts between confined bubble moving back and forth along the channels. For $G = 83$ kg/m^2 s, a sharp increase in heat transfer coefficient is observed at low qualities ($x_e < 0.2$), whereas for higher qualities h_{tp} initially slightly increases with x_e, and drops slightly after the exit quality exceeds 0.47. While a similar trend is observed for $G = 166$ kg/m^2 s at low qualities, at higher qualities the heat transfer coefficient displays a continuous decline with exit quality until dry-out condition is reached. At $G = 302$ kg/m^2 s, h_{tp} monotonically decreases with exit quality over the entire range.

4.2.1. Comparison with existing correlations

The two-phase heat transfer coefficients obtained in the current study are compared with eight published and two new (developed through the results of this study) empirical correlations. The results are summarized in Table 2. Four correlations (1, 2, 3, 4) have been developed based on results from minichannels, one from microchannels (5) and the remaining from conventional scale channels. Correlation (1), (2), (4), (5), (6a), and (9) are for nucleate boiling, (3), (6b), and (10) for convective flow, and (7) and (8) for both. Comparisons between experimental heat transfer coefficients and the predictions of minichannel and microchannel correlations are presented in Figs. 9 and 10. Similar to Qu and Mudawar [4] the correlations of Lazarek and Black [28], Tran et al. [29], and Yu et al. [30] overpredict most of the experimental data. It should be noted however that they are recommended for channel size more than 10 times larger than the microchannels in this study. The only correlation that has been specifically developed for microchannels [31] underpredicted the results within 48.5% (MAE). This might suggest that reentrant cavity surfaces do in

Table 2
Two-phase heat transfer coefficient correlations

Correlation number	Reference	Recommended channel size and heat transfer mechanism	Correlation	MAE (%)
1	Lazarek and Black [28]	Circular, $d_h = 3.15$ mm Nucleate boiling	$h_{tp} = 30F(Re_{LO})^{0.857}Bo^{0.714}\frac{k_F}{d_h}$	101.9
2	Tran et al. [29]	Circular, $d_h = 2.46$ mm Rectangular $d_h = 2.4$ mm Nucleate boiling	$h_{tp} = 8.4 \times 10^5 F(Bo^2 We_F)^{0.3}\left(\frac{\rho_F}{\rho_G}\right)^{-0.4}$	80.9
3	Lee and Lee [32]	Rectangular, $d_h = 0.78$–3.63 mm Convective boiling	$h_{tp} = \frac{F}{x_e}\int_0^{x_e} 10.3\beta^{0.398}\phi_F^{0.598}h_{sp}\,dx$ $\phi_F = \left(1 + \frac{C}{X_{vt}} + \frac{1}{X_{vt}^2}\right), \quad C = 6.185 \times 10^{-2}Re_{Lo}^{0.726}$ $X_{vt} = \left(\frac{f_F}{f_G}\right)^{0.5}\left(\frac{1-x}{x}\right)\left(\frac{\upsilon_f}{\upsilon_G}\right)^{0.5}, \quad f_G = \frac{0.079}{Re_G^{0.25}}, \quad Re_G = \frac{Gd_h x}{\mu_G}$ $f_F = \frac{24}{Re_F}(1 - 1.355\beta + 1.947\beta^2 - 1.701\beta^3 + 0.953\beta^4 - 0.254\beta^5)$ $h_{sp} = 8.235(1 - 2.042\beta + 3.085\beta^2 - 2.477\beta^3 + 1.058\beta^4 - 0.186\beta^5)\frac{k_F}{d_h}$	608
4	Yu et al. [30]	Circular, $d_h = 2.98$ mm Nucleate boiling	$h_{tp} = 6.4 \times 10^6 F(Bo^2 We_F)^{0.24}\left(\frac{\rho_F}{\rho_G}\right)^{-0.2}$	48.5
5	Warrier et al. [31]	5 parallel rectangular channels, $d_h = 0.75$ mm Nucleate boiling	$h_{tp} = \frac{F}{x_e}\int_0^{x_e}\left(1 + 6Bo^{1/16} - 5.3(1 - 855Bo)x^{0.65}\right)h_{sp}\,dx$ where $h_{sp} = 8.235(1 - 2.042\beta + 3.085\beta^2 - 2.477\beta^3 + 1.058\beta^4 - 0.186\beta^5)\frac{k_F}{d_h}$	48.4
6a	Kandlikar [33]	Conventional channels Nucleate boiling	$h_{tp} = \frac{F}{x_e}\int_0^{x_e}(0.6683Co^{-0.2}(1-x)^{0.8}h_{LO} + 1058.0Bo^{0.7}(1-x)^{0.8}h_{LO})\,dx$ where $h_{LO} = 0.023(Re_F)^{0.8}(Pr_F)^{0.4}\frac{k_F}{d_h}$	32.7

6b	Kandlikar [33]	Conventional channels Convective boiling	$h_{tp} = \frac{F}{x_e}\int_0^{x_e}(1.136Co^{-0.9}(1-x)^{0.8}h_{LO} + 667.2Bo^{0.7}(1-x)^{0.8}h_{LO})\,dx$ where $h_{LO} = 0.023(Re_F)^{0.8}(Pr_F)^{0.4}\frac{k_F}{d_h}$	29.4
7	Liu and Winterton [35]	Conventional channel Nucleate and convective boiling	$h_{tp} = \frac{F}{x_e}\int_0^{x_e}\left((Eh_{LO})^2 + (Sh_{pool})^2\right)^{0.5}dx$ where $h_{LO} = 0.023(Re_F)^{0.8}(Pr_F)^{0.4}\frac{k_F}{d_h},\quad E = \left(1 + xPr_F\left(\frac{\rho_F}{\rho_G} - 1\right)\right)^{0.35}$ $S = (1 + 0.055E^{0.1}Re_{LO}^{0.16})^{-1},\quad h_{pool} = 55\left(\frac{p}{p_{cr}}\right)^{0.12}\left(-\log_{10}\left(\frac{p}{p_{cr}}\right)\right)^{-0.55}M_W^{-0.5}q''^{0.67}$	50.9
8	Steiner and Taborek [36]	Conventional channel Nucleate and convective boiling	$h_{tp} = \frac{F}{x_e}\int_0^{x_e}((F_{tp}h_{LO})^3 + (F_{nb}h_{nb})^3)^{1/3}\,dx$ where $h_{LO} = 0.023(Re_F)^{0.8}(Pr_F)^{0.4}\frac{k_F}{d_h},\quad F_{tp} = \left((1-x)^{1.5} + 1.9x\left(\frac{\rho_F}{\rho_G}\right)^{0.35}\right)^{1.1}$ $F_{nb} = 0.72\left(2.816P_r^{0.45} + \left(3.4 + \frac{1.7}{1-P_r^7}\right)P_r^{3.7}\right)\left(\frac{q''}{1.5\times10^5}\right)^{(0.8-0.1\exp(1.75P_r))}\left(\frac{d_h}{0.01}\right)^{-0.4}$ $h_{nb} = 25,580\ \mathrm{W/m^2\,K}$	71.9
9	Current study	5 parallel rectangular channels, $d_h = 0.223$ mm Nucleate boiling	$h_{tp} = 1.068(q'')^{0.64}\quad [\mathrm{in\ W/m^2\,K}]$	17.5
10	Current study	5 parallel rectangular channels, $d_h = 0.223$ mm Convective boiling	$h_{tp} = 4.068\times10^4(Re_{LO})^{0.12}(1-x_e)^{0.8}\left(\frac{1-x_e}{x_e}\right)^{0.02}\quad [\mathrm{in\ W/m^2\,K}]$	8.9

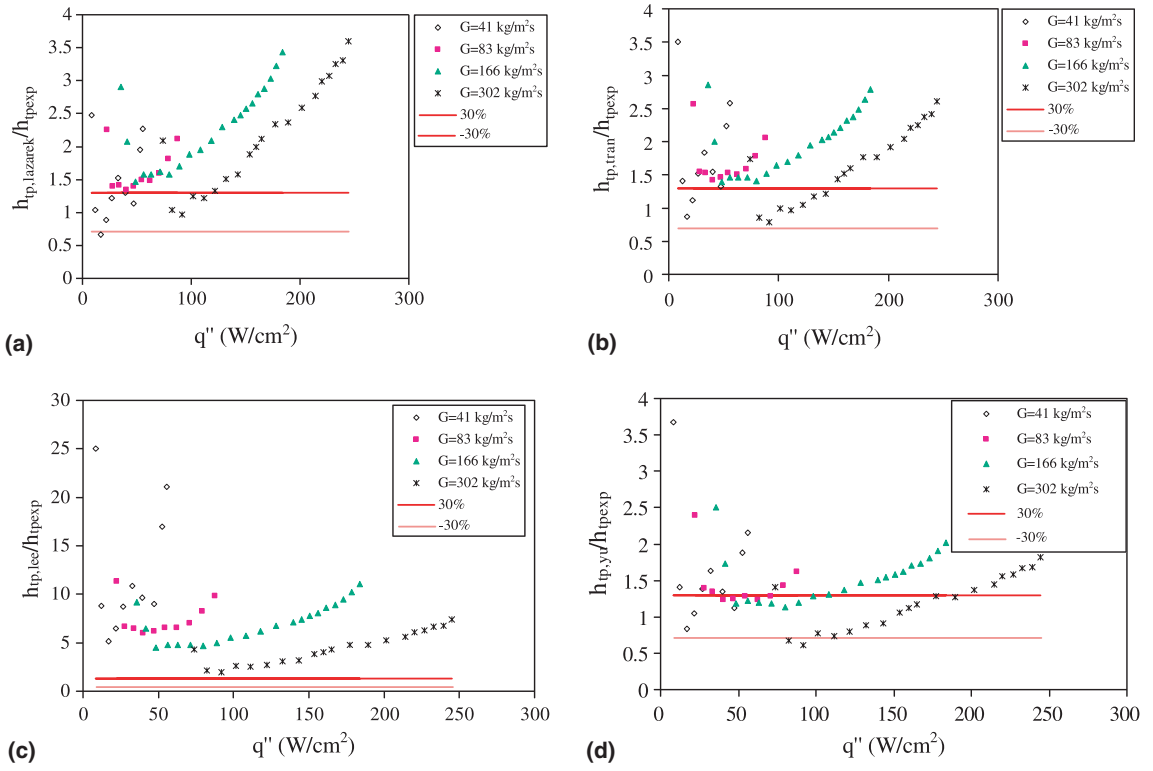

Fig. 9. Predictions of Correlations 1 to 4 (a–d).

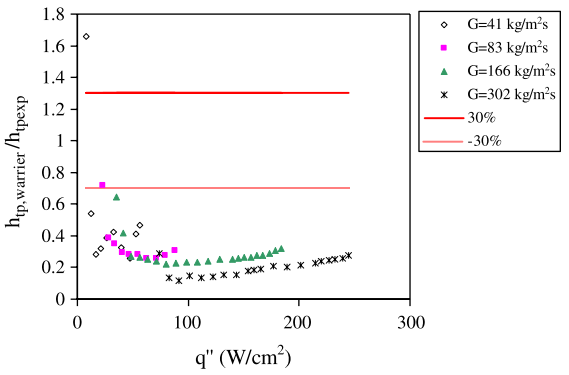

Fig. 10. Predictions of Correlation 5.

fact provide significant enhancement at least with respect to the heat transfer coefficient. The correlation of Lee and Lee [32], recommended for convective boiling, excessively overpredicted the results by 608% (MAE). This might be because turbulent flow is assumed, while the Reynolds numbers in the current study are well below the laminar-turbulent transition value.

Although Kandlikar correlation [33] has been developed for conventional scale channels it has been used in various studies such as Qu and Mudawar [4] and Wambsganns et al. [34] to correlate microchannel and minichannel boiling flow with moderate agreement. Generally, the correlation overpredicted the results. For example, the correlation overpredicted Qu and Mudawar [4] heat transfer coefficients by up to 300%. The prediction of the nucleate and convective versions of the Kandlikar correlation are shown in Fig. 11a and b, respectively, for the entire set of experimental data. Since a portion of the data agrees well with the correlations, the data is further divided into two sets: one for low heat fluxes and low to moderate mass velocities (which is designated as dominated by nucleate boiling in the following section) and the other for high heat fluxes and moderate to high mass velocities (designated in the subsequent section as convective boiling dominated). As can be seen in Fig. 12a and b the nucleate boiling version of the correlation for the most part underpredicts the data for $G = 41$ and 83 kg/m^2 s with MAE of 25.2%, while it overpredicts the data for $G = 166$ kg/m^2 s by 35.0%. The prediction of the convective version of the correlation to the experimental data, which has been designated as dominated by convective boiling, has an MAE of 36.78% (Fig. 12d), while the prediction of the nucleate boiling experimental data has an MAE of 40.29% (Fig. 12c). Although the agreement of the moderate to high mass velocities to the correlation

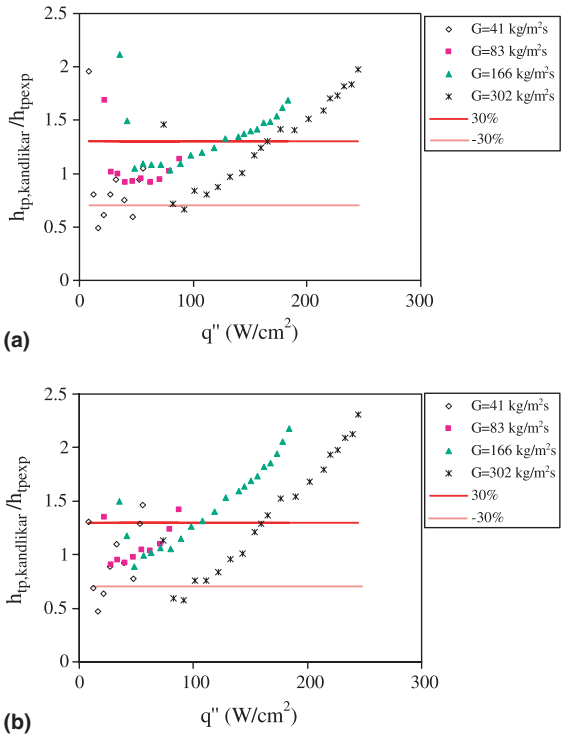

Fig. 11. Predictions of Correlations 6a (a) and 6b (b) [entire data].

is reasonably well with respect to the MAE value, the h_{tp} trend is not well captured. On the other hand, the h_{tp} does follow the correlation trend at low to moderate mass velocities. The correlations of Liu and Winterton [35] and Steiner and Taborek [36] considerably underpredicted all the data (Fig. 13a and b). This could be associated with the reentrant cavities, which may have provided enhancement in heat transfer coefficient. It should be noted, however, that Steiner and Taborek correlations agreed very well with h_{tp} trend and showed consistent error throughout most of applied heat fluxes.

In general the agreement of the current experimental results is not within satisfactory limits. There are very limited correlations for microchannels and deviations between existing data, and available correlations are relatively large and inconsistent. The correlations developed for microchannels considerably underpredicted the experimental data, while, similar to other microchannel studies, minichannel correlations considerably overpredicted the data. Therefore, at this point it is difficult to make good quantitative conclusions regarding the capabilities of reentrant cavities in enhancing heat transfer coefficient. However, the foregoing discussion and heat transfer coefficients trends provide valuable clues to assess the dominant boiling mechanism.

4.3. Nucleate versus convective boiling

The debate on the heat transfer mechanism predominating boiling in microchannels has still not been fully resolved. Kandlikar [7] has been strongly advocating that nucleate boiling is the dominating mechanism governing boiling in microchannels, whereas Qu and Mudawar [4] provided supporting evidence of convective dominant. While making his arguments, Kandlikar states that experimental results from various mini channel investigation [32,24] of two-phase heat transfer coefficient are well correlated with conventional scale nucleate boiling dominant correlations. He also stresses that flow visualizations made by various researchers reveal that flow patterns in microchannels exhibit transient characteristics similar to a bubble ebullition cycle, which is distinctive in nucleate boiling. Two dimensionless parameters are said to be indicative of nucleate boiling: the k_1 and the Reynolds number. Although no numerical value is given for k_1 in which the flow transits from one mechanism to another it is argued that higher k_1 values and $Re_{LO} < 300$ (from [37]) correspond to nucleate boiling dominant region. Qu and Mudawar [4] on the other hand, make their argument based on the dependence of the two-phase heat transfer coefficient on heat flux, liquid subcooling, mass velocity, and mass quality. The Boiling number, Bo, is given as the criterion to identify the dominant flow pattern, where low Boiling numbers correspond to a convective dominant mechanism. Two-phase heat transfer coefficient during nucleate boiling typically increases with heat flux, and is independent of liquid subcooling, mass velocity and mass quality. Convective boiling heat transfer coefficient, on the other hand, increases with quality and mass velocity, but is weakly dependent on heat flux.

In the present study the Reynolds number range is lower than 300 and the k_1 are above 1.4×10^{-3} which by Kandlikar criteria is clearly well within the nucleate boiling dominant region. The Boiling number is in the range of 3.65×10^{-4}–6.3×10^{-3} which according to Lazarek and Black [28] and Wambsganns et al. [34] is in the nucleate boiling region. In the foregoing discussion various aspects, namely the dependence of the heat transfer coefficient on the thermo-hydraulic conditions and the agreement with available nucleate or convective dominant correlation, which provide clues for the governing boiling mechanism have been examined and summarized in Table 3.

(a) *Effect of heat flux*

The data provided in Fig. 7 can be classified into three regions of heat flux dependence: (i) increasing h_{tp} with heat flux, (ii) h_{tp} independent of heat flux, (ii) decreasing h_{tp} with heat flux. For low mass velocity a consistent trend of increasing h_{tp} with heat flux is notable, while the heat transfer coefficient for the high mass velocity ($G = 302$ kg/m^2 s) monotonically declines with

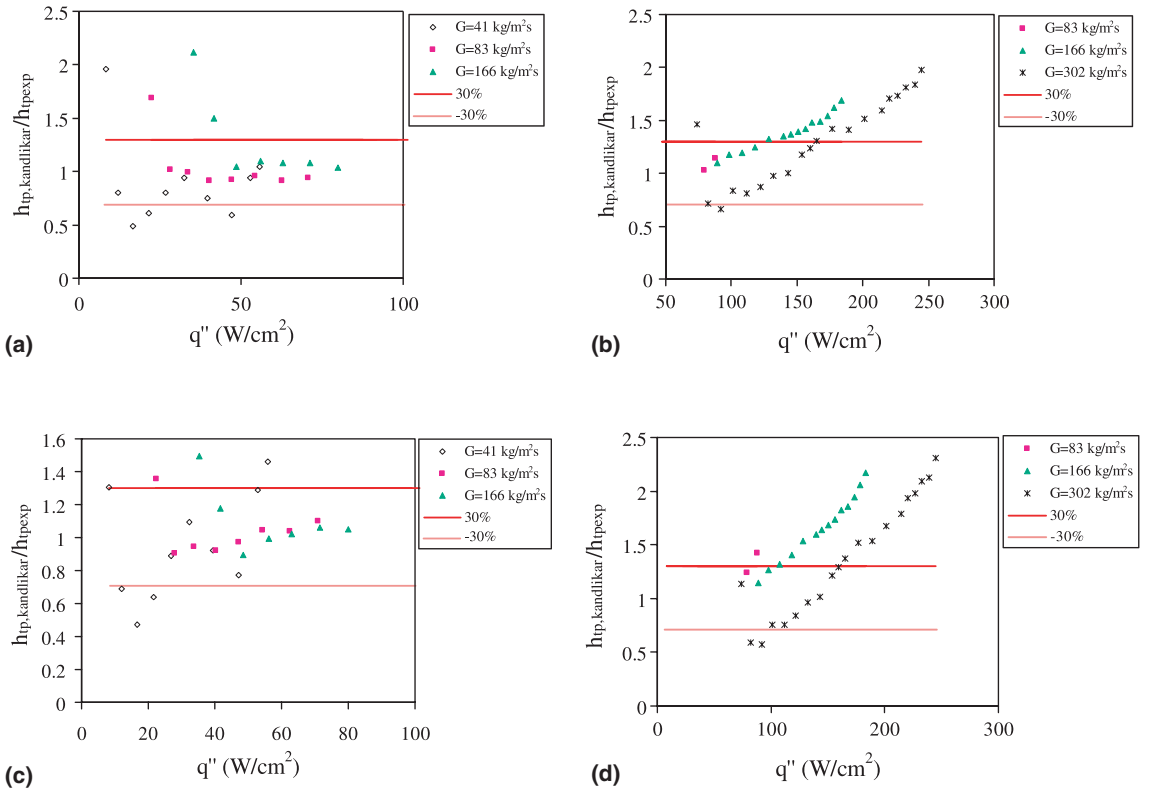

Fig. 12. Predictions of nucleate and convective boiling data provided by Correlations 6a (a,b) and 6b (c,d) [(a,c) nucleate boiling data; (b,d) convective boiling data].

q''. For moderate mass velocity ($G = 166$ kg/m^2 s) the heat transfer initially increases with q'' and then reaches a plateau. As far as the dependence on heat flux the data strongly suggests that at low mass velocities and all heat fluxes (up to CHF) and moderate mass velocities under low heat fluxes nucleate boiling dominates, while for moderate mass velocities under high heat fluxes and high mass velocities under all heat fluxes convective boiling dominates.

(b) *Effect of mass velocity*

Although the data for $G = 41$ kg/m^2 s is somewhat scattered, the heat transfer coefficient for all heat fluxes at low mass velocities and moderate mass velocities under low heat fluxes does not seem to be strongly dependent on the mass velocity. However, a significant increase is observed when the mass velocity is increased to 302 kg/m^2 s. This again supports the existence of nucleate boiling at low mass velocities and convective boiling at high mass velocities.

(c) *Effect of exit quality*

From Fig. 8 it is evident that h_{tp} is weakly dependent on the exit quality for moderate mass velocities and low to moderate qualities, and for low flow rates prior to CHF conditions, indicating nucleate boiling dominating mechanism. At moderate mass velocities with high qualities and high mass velocities for all mass qualities the heat transfer coefficient decreases with x_e. As noted by Qu and Mudawar [4], this is not a characteristic of conventional boiling flows. However, various studies [4,7,31,34] have reported similar trend in microchannel boiling.

From the aforementioned discussion it is clear that as mass velocity increases the boiling mechanism tendency to transition from a nucleate to a convective dominant mechanism increases. Furthermore, convective boiling tends to predominate as heat flux increases. Since the Reynolds and Boiling numbers have been previously suggested as criteria which determine the boiling mechanism, a flow map based on these two dimensionless parameters is shown in Fig. 14. The identification of the boiling mechanism of each data point is based on the observed trends of h_{tp} in Figs. 7 and 8. Emphasis is given to points where the heat transfer coefficient stops increasing and a continuous or a sudden decrease begins. The data for low mass velocities ($G = 41$ and 83 kg/m^2 s) are considered to be included in the nucleate dominant region except the last two data points, which apparently correspond to dry-out conditions. The data for the moderate mass velocity ($G = 166$ kg/m^2 s) at low heat flux ($q'' < 88$ W/cm^2) is included in the nucleate

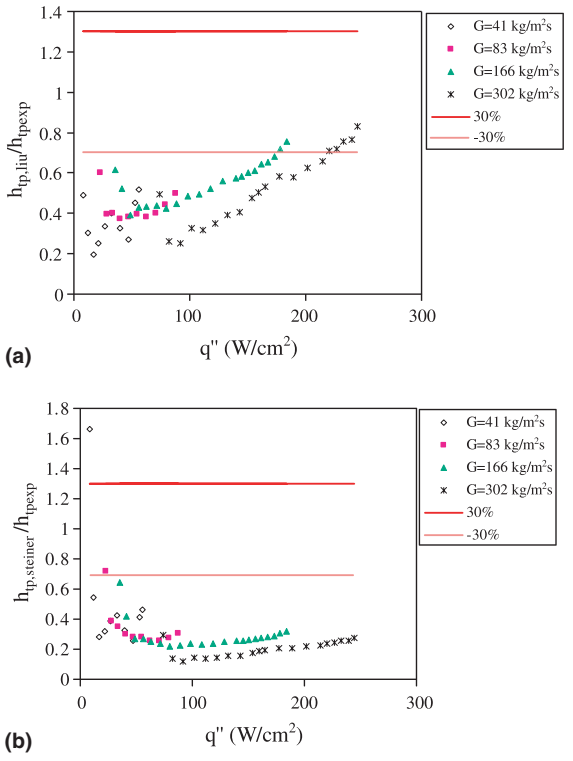

Fig. 13. Predictions of Correlations 7 (a) and 8 (b).

boiling region, whereas all the remaining data (the other portion of $G = 166\ \mathrm{kg/m^2\,s}$ and $G = 302\ \mathrm{kg/m^2\,s}$) is considered to be convective boiling dominant.

As can clearly be seen, low *Bo* and low *Re* correspond to nucleate boiling dominated boiling flow, while high *Bo* and high *Re* promote convective boiling. While the critical Reynolds number for transition is below 300, the increasing dominance of nucleate boiling at low Reynolds number is in accordance with Kandlikar and Balasubramanian [37]. Although, the flow map clearly shows the dependence of the boiling mechanism on the Boiling number as indicated by Qu and Mudawar it does deviate from their suggested trend (lower Boiling number associated with convective boiling). However, further examination of their argument, which is based on earlier work, does suggest that higher heat fluxes correspond to convective boiling. The flow mechanism transition can be readily obtained from the map. The linear relation between the Boiling and Reynolds number provides a simple measure for the transition criteria in the following form:

$$Re_{\mathrm{cr}} = 163.59 - 2.73 \times 10^4 Bo. \tag{16}$$

It should be noted that other dimensionless parameters (especially those that are connected with the surface tension forces, such as the Weber or Capillary numbers) might be of significant importance, and can provide

Table 3
Major features of boiling mechanisms and findings of this study

Parameter	G	q''	x_e	Bo	k_I	Flow pattern
Nucleate boiling	h_{tp} is weakly dependent on G (slight increase)	$h_{tp} \propto q''^{const}$ strong dependence	h_{tp} is weakly dependent on G	Low Boiling number Low Re_{LO}	High k_I	Single and confined bubble
Convective boiling	h_{tp} is strongly dependent on G	h_{tp} is weakly dependent on q''	h_{tp} is weakly dependent on G (decreasing trend)	High Bo High Re_{LO}	Low k_I	Annular
Current study	$G = 41\ \mathrm{kg/m^2\,s}$, $G = 83$ and $166\ \mathrm{kg/m^2\,s}$, and for 41 W/cm^2 $< q'' <$ 71 W/cm^2	$G = 83$ and $166\ \mathrm{kg/m^2\,s}$, and for q'' (41–71 Wc/m^2)	$G = 83$ and $166\ \mathrm{kg/m^2\,s}$, and for q'' (41–71 W/cm^2)	High Bo (3.65×10^4 $< Bo < 6.3 \times 10^{-3}$)	High k_I (1.4×10^3 $< k_I < 3.47 \times 10^{-2}$)	$G = 83$ and $166\ \mathrm{kg/m^2\,s}$, and for q'' (41–71 W/cm^2)
	Weak dependence $G = 83$ and $166\ \mathrm{kg/m^2\,s}$, and $q'' > 71$ W/cm^2	Strong dependence $G = 83$ and $166\ \mathrm{kg/m^2\,s}$, and $q'' > 71$ W/cm^2	Weak dependence $G = 83$ and $166\ \mathrm{kg/m^2\,s}$, and $q'' > 71$ W/cm^2			Confined bubble $G = 83$ and $166\ \mathrm{kg/m^2\,s}$, and $q'' > 71$ W/cm^2
	Moderate dependence $G = 302\ \mathrm{kg/m^2\,s}$	Moderate dependence $G = 302\ \mathrm{kg/m^2\,s}$	Strong dependence $G = 302\ \mathrm{kg/m^2\,s}$			Annular $G = 302\ \mathrm{kg/m^2\,s}$
	Moderate dependence	Moderate dependence $G = 41\ \mathrm{kg/m^2\,s}$ No conclusion can be drawn	Strong dependence $G = 41\ \mathrm{kg/m^2\,s}$ No conclusion can be drawn			Annular $G = 41\ \mathrm{kg/m^2\,s}$ Intermittent annular

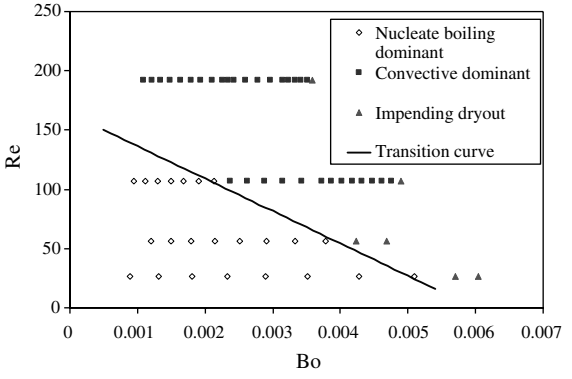

Fig. 14. Flow map.

additional insight to the physical phenomena deriving the thermal-hydraulic mechanism. However, experiments have been performed with water and currently insufficient data is available to form reliable transition correlations, which account for the Weber number, along with other possible dimensionless parameters.

4.3.1. Development of nucleate and convective boiling correlation

A direct result of the flow map is the realization that a correlation that considers the nucleate boiling or the convective boiling mechanism alone is insufficient to relate the entire data obtained in the current study. It is rationale to either use a more universal correlation of the Kandlikar type or use a correlation for each region of dominance. Stephan and Abdelsalam [38] type corre-

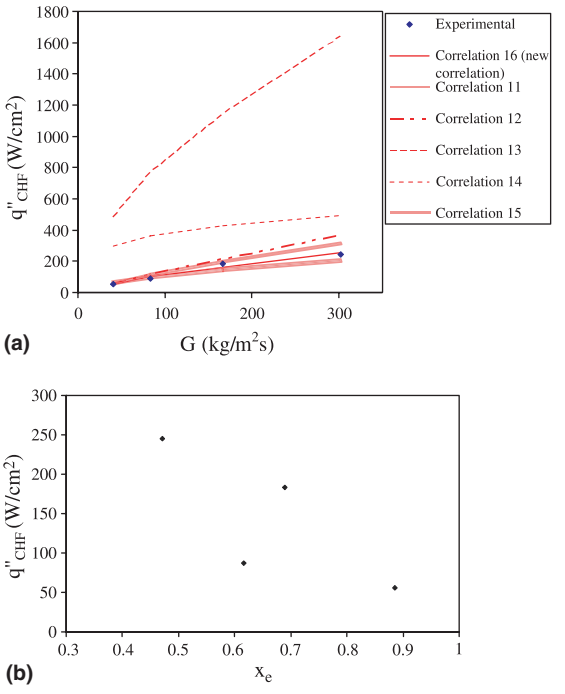

Fig. 16. CHF data in this study and predictions of correlations: (a) q''_{CHF} versus G and (b) q''_{CHF} versus x_e.

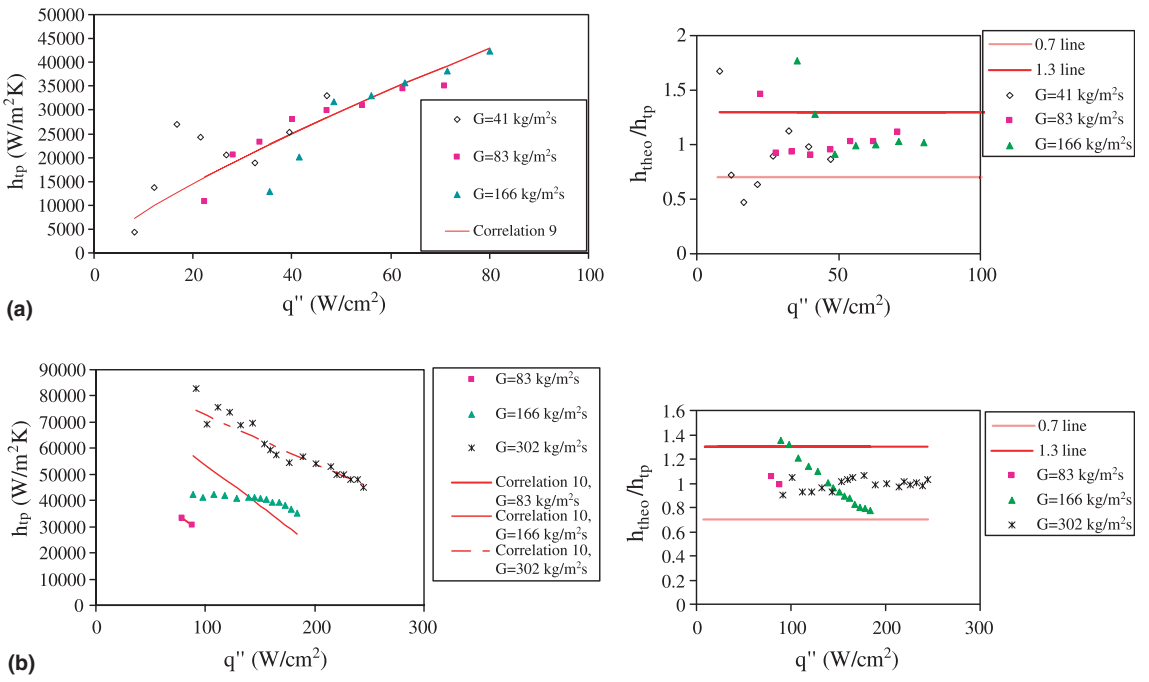

Fig. 15. Predictions of Correlations 9 (a) and 10 (b).

lation, listed in Table 2 (correlation 9), recommended for nucleate boiling is modified to represent the experimental data for $Re < Re_{cr}$. The method of least squares has been employed in fitting the experimental data and resulted in the following correlation:

$$h_{tp} = 1.068(q'')^{0.64} \quad [\text{in W/m}^2\,\text{K}]. \tag{17}$$

As shown in Fig. 15a the agreement between experiments and the correlation resulted in MAE of 17.5%. When excluding the $G = 41$ kg/m^2 s data (which is somewhat scattered) the correlation predicts the data with MAE of 10.6%. The excellent agreement reinforces the assessment that nucleate boiling is indeed prevailing for Reynolds number below the critical value.

For $Re > Re_{cr}$, the following correlation in the form of the Kandlikar's convective term correlation [33] was used to correlate the experimental data:

$$h_{tp} = 4.068 \times 10^4 (Re_{LO})^{0.12} \times (1 - x_e)^{0.8} \left(\frac{1 - x_e}{x_e}\right)^{0.02} \quad [\text{in W/m}^2\,\text{K}]. \tag{18}$$

As shown in Fig. 15b the prediction is excellent with MAE of 8.9%, indicating convective boiling dominance.

4.4. Critical heat flux

Critical heat flux condition is reached for all mass fluxes once a significant increase in the wall temperature has been detected upon a slight increase in the power delivered to the device. As shown in Fig. 16, the dependence of CHF on the mass velocity and heat flux are evident, and are in accordance with many conventional scale correlations' trends [39]. That is CHF increases with G and decreases with x_e. Furthermore, as detailed

Table 4
CHF correlation

Correlation number	Reference	Recommended channel size and fluid	Correlation	MAE (%)
11	Bowring [40]	Circular, conventional channels	$q''_{CHF} = \frac{A' + d_h G(h_F - h_i)/4}{C' + L}$ $A' = \frac{0.579 F_{B1} d_h G h_{FG}}{1.0 + 0.0143 F_{B2} d_h^{1/2} G}$ $C' = \frac{0.077 F_{B3} d_h G}{1.0 + 0.347 F_{B4} (G/1356)^n}$ $n = 2.0 - 0.00725p$	14.9
12	Katto and Ohne [41]	Circular, conventional channels	$q''_{CHF} = XG(h_{FG} + K(\Delta h_{sub})_i)$ where $X = \frac{0.098(\rho_G/\rho_F)^{0.133} \left(\frac{\sigma\rho_F}{G^2 L}\right)^{0.433} (L/d_h)^{0.27}}{1.0 + 0.0031(L/d_h)}$ $K = \frac{0.261}{0.25\left(\frac{\sigma\rho_F}{G^2 L}\right)^{0.0433}}$	20.0
13	Bowers and Mudawar [5]	Square, $d_h = 2$ mm R-113	$q'' = 0.16 G h_{FG} We^{-0.19} \left(\frac{L}{d_h}\right)^{-0.54}$	643
14	Ammerman and You [42]	Rectangular, $d_h = 0.78$–3.63 mm FC-87	$q''_{CHF} = 0.52 G h_{FG} We^{-0.37} \left(\frac{\rho_G}{\rho_L}\right)^{0.6} (-x_i)^{0.1}$	244
15	Qu and Mudawar [43]	Rectangular, $d_h = 0.38$–2.54 mm R-113, water	$q''_{CHF} = 33.43 G h_{FG} We^{-0.21} \left(\frac{\rho_G}{\rho_L}\right)^{1.1} \left(\frac{L}{d_h}\right)^{-0.36}$	17.1
16	Current study	5 parallel rectangular channels, $d_h = 0.223$ mm Convective boiling	$q''_{CHF} = 0.0035 G h_{FG} We^{-0.12}$	7.4

in Table 4, comparison of current data to large scale correlations shows good agreement with the correlation developed based on water boiling studies. For example, Bowring [40] correlation predicted the data with MAE of 14.7%, while Katto and Ohne [41] correlation had a MAE of 20.0%. The correlation of Qu and Mudawar [43] developed for mini-and microchannels also provided a good prediction of the experimental data (MAE = 17.1%). From Table 4 it is also notable that Ammerman and You [42] and Bowers and Mudawar [5] correlation provided excessive overprediction of the data, primarily because they were developed for refrigerants possessing vastly different properties than water. In fact, these two correlations provided CHF values corresponding to superheated vapor.

In order to further improve the representation of the experimental data a correlation having a similar form of the Bowers and Mudawar [5] correlation has been developed. The correlation predicted the data with a MAE of 7.4% and has the following form:

$$q''_{\mathrm{CHF}} = 0.0035 G h_{\mathrm{FG}} We^{-0.12}. \quad (19)$$

5. Conclusions

In this study, boiling heat transfer experiments in flow through microchannels with reentrant cavities have been conducted. In the light of these experiments, governing heat transfer mechanisms have been identified and evaluated for different operating conditions. Moreover, the trends for Critical Heat Flux have been investigated at different mass flux and exit qualities. The main conclusions drawn from this study are presented below:

- It is difficult to draw any quantitative conclusions regarding the capabilities of reentrant cavities, such as the ones presented in this paper, to enhance heat transfer, since deviations between existing data and available correlations are relatively large and inconsistent. Furthermore, there is still a disagreement within the heat transfer community on the dominant boiling mechanism in microchannels. Therefore, a comparison of the current results with available microchannels boiling literature will not assist in determining the potential of reentrant cavities to promote nucleate boiling. However, there are extremely limited critical heat flux data and correlations, which pose additional difficulties once comparison attempt is made. To better evaluate the capabilities inherent in reentrant cavities for enhancing heat transfer in microchannels, it is imperative to perform experiments on two microchannel devices with identical global geometrical configurations, i.e., one having reentrant cavities and one with plain smooth walls.
- Depending on the mass velocity, and heat flux, both nucleate and convective dominant boiling mechanisms have been detected. A transition between nucleate and convective boiling is apparent, and has been quantified in terms of the Reynolds and the Boiling number. Nucleate boiling is dominant for low *Re* and *Bo*. A flow map has been developed to distinguish two regions with convective and nucleate boiling dominance.
- Experimental heat transfer coefficients show trends similar to the predictions of nucleate dominant correlations pertinent to minichannels for nucleate boiling dominant zone of the data. However, the magnitudes displayed large deviations.
- Among the correlations used to represent the experimental data, Kandlikar correlation [33] provided the best prediction. Two correlations were developed to represent the experimental data for both nucleate boiling and convective boiling dominant regions.
- CHF data has been compared with conventional as well as minichannel correlations. Conventional correlations correlated the experimental data within reasonable agreement. The CHF correlation, which best fits the experimental results, has been specified.

Acknowledgements

Graduate student support from Rensselaer Polytechnic Institute is gratefully acknowledged. The microfabrication was performed at the Cornell NanoScale Facility (a member of the National Nanotechnology Infrastructure Network), which is supported by the National Science Foundation under Grant ECS-0335765, its users, Cornell University and industrial affiliates. The authors thank Mr. C. Mishra for his contribution in fabricating the MEMS device and his guidance in experiments and visualizations.

References

[1] L. Jiang, M. Wong, Y. Zohar, Forced convection boiling in microchannel heat sink, J. Microelectromech. Syst. 10 (1) (2001) 80–87.
[2] S.G. Kandlikar, Fundamental issues related to flow boiling in minichannels and microchannels, Exp. Thermal Fluid Sci. 26 (2002) 389–407.
[3] S.G. Kandlikar, Two-phase flow patterns, pressure drop, and heat transfer during Boiling in minichannels flow passages of compact evaporators, Heat Transfer Eng. 23 (1) (2002) 5–23.
[4] W. Qu, I. Mudawar, Flow boiling heat transfer in two-phase micro-channel heat sink—I. Experimental investigation and assessment of correlation methods, Int. J. Heat Mass Transfer 46 (15) (2003) 2755–2771.

[5] M.B. Bowers, I. Mudawar, High flux boiling in low flow rate, Low pressure drop mini-channel and micro-channel heat sinks, Int. J. Heat Mass Transfer 37 (2) (1994) 321–334.
[6] M.E. Steinke, S.G. Kandlikar, An experimental investigation of flow boiling characteristics of water in parallel microchannels, J. Heat Transfer 126 (4) (2004) 518–526.
[7] S.G. Kandlikar, Heat transfer mechanisms during flow boiling in microchannels, J. Heat Transfer 126 (1) (2004) 8–16.
[8] K. Mohrlok, K. Spindler, E. Hahne, Pool boiling heat transfer of R134a-oil mixture on a smooth tube and an enhanced tube, in: Proceedings 3rd European Thermal Science Conference, vol. 2, 2000, pp. 785–790.
[9] R. Mertz, A. Wein, M. Groll, Experimental investigation of flow boiling heat transfer in narrow channels, Int. J. Heat Technol. 14 (2) (1996) 47–54.
[10] R. Mertz, M. Groll, B. Thonon, Tubular heat transfer elements for compact two-phase heat exchangers, in: 2nd International Conference On Compact Heat Exchangers and Enhancement Technology for the Process Industries, Banff, Canada, 1999.
[11] R. Mertz, M. Groll, On boiling heat transfer in narrow channels, Int. J. Heat Technol. 18 (1) (2000) 75–79.
[12] R. Mertz, R. Kulenovic, P. Schafer, M. Groll, Boiling of hydrocarbons on tubes with subsurface structures, in: 3rd International Conference on Compact Heat Exchangers and Enhancement Technology for the Process Industries, Davos, Switzerland, 2001.
[13] R. Mertz, R. Kulenovic, Y. Chen, Y., M. Groll, Pool boiling of butane from enhanced evaporator tubes, in: 12th International Heat Transfer Conference, Grenoble, France, 2002.
[14] R. Roser, B. Thonon, P. Mercier, Experimental investigations on boiling of *n*-pentane across an horizontal tube bundle: two-phase flow and heat transfer characteristics, Int. J. Refrig. 22 (1999) 536–547.
[15] B. Thonon, Enhanced reboilers for the process industry, in: 3rd International Conference On Compact Heat Exchangers and Enhancement Technology for the Process Industries, Davos, Switzerland, 2001.
[16] L. Aprin, P. Mercier, L. Tadrist, Analysis of experimental results of *n*-pentane and propane boiling across an horizontal tube bundle, in: 12th International Heat Transfer Conference, Grenoble, France, 2002.
[17] J.P. O'Connor, S.M. You, A painting technique to enhance pool boiling heat transfer in saturated FC-72, ASME J. Heat Transfer 117 (1995) 387–393.
[18] J.Y. Chang, S.M. You, Boiling heat transfer phenomena from micro-porous surfaces in saturated FC-72, Int. J. Heat Mass Transfer 40 (18) (1997) 4437–4447.
[19] J.Y. Chang, S.M. You, Enhanced boiling heat transfer from micro-porous surfaces: effect of coating composition and method, Int. J. Heat Mass Transfer 40 (1997) 4449–4460.
[20] M. Jakob, Heat Transfer, Wiley, New York, 1949, pp. 636–638.
[21] R.L. Webb, The evolution of enhanced surface geometries for nucleate boiling, Heat Transfer Eng. 2 (3–4) (1981) 46–69.
[22] R.L. Webb, Nucleate boiling on porous coated surfaces, Heat Transfer Eng. 4 (3–4) (1983) 71–82.
[23] P. Griffith, J.D. Wallis, The role of surface conditions in nucleate boiling, Chem. Eng. Prog. Symp. 56 (49) (1960) 49–63.
[24] J.E. Benjamin, J.W. Westwater, Bubble growth in nucleate boiling of binary mixture, in: International Development in Heat Transfer, ASME, New York, 1961, pp. 212–218.
[25] J.M. Yatabe, J.W. Westwater, Bubble growth rates for ethanol–water and ethanol–isoproponal mixture, Chem. Eng. Prog. Symp. 62 (64) (1966) 17–23.
[26] C.F. Gottzmann, J.B. Wulf, P.S. O'neill, Theory and application of high performance boiling surfaces to components of absorption cycle air conditioners, in: Proceedings Conference National gas Research Technology, Session V, Paper 3, Chicago, February 28, 1971.
[27] S. Kline, F.A. McClintock, Describing uncertainties in single-sample experiments, Mech. Eng. 75 (1) (1953) 3–8.
[28] G.M. Lazarek, S.H. Black, Evaporative heat transfer, pressure drop and critical heat flux in a small diameter vertical tube with R-113, Int. J. Heat Mass Transfer 25 (7) (1982) 945–960.
[29] T.N. Tran, M.W. Wambsganns, D.M. France, Small circular-and rectangular-channel boiling with two refrigerants, Int. J. Multiphase Flow 22 (3) (1996) 485–498.
[30] W. Yu, D.M. France, M.W. Wambsgans, J.R. Hull, Two-phase pressure drop, boiling heat transfer, and critical heat flux to water in a small-diameter horizontal tube, Int. J. Multiphase Flow 28 (6) (2002) 927–941.
[31] G.R. Warrier, V.K. Dhir, L.A. Momoda, Heat transfer and pressure drop in narrow rectangular channel, Exp. Therm. Fluid Sci. 26 (2002) 53–64.
[32] H.J. Lee, S.Y. Lee, Heat transfer correlation for boiling flows in small rectangular horizontal channels with low aspect ratios, Int. J. Multiphase Flow 27 (12) (2001) 2043–2062.
[33] S.G. Kandlikar, A general correlation for saturated two-phase boiling heat transfer inside horizontal and vertical tubes, J. Heat Transfer 112 (1) (1990) 219–228.
[34] M.W. Wambsganns, J.A. Jendrzejczyk, D.M. France, T.N. Tran, Boiling heat transfer in a small diameter tube, J. Heat Transfer 115 (4) (1993) 963–972.
[35] Z. Liu, R.H.S. Winterton, A general correlation for saturated and subcooled flow boiling in tubes and annuli, based on a nucleate pool boiling equation, Int. J. Heat Mass Transfer 34 (1991) 2759–2766.
[36] D. Steiner, J. Taborek, Flow boiling heat transfer in vertical tubes correlated by asymptotic model, Heat Transfer Eng. 13 (1992) 43–69.
[37] S.G. Kandlikar, P. Balasubramanian, Extending the applicability of the flow boiling correlation at low Reynolds number flows in micro-channels, in: Presented at the First International Conference on Microchannels and Minichannels, Paper ICMM2003-1075, ASME, New York, 2003, pp. 603–608.
[38] K. Stephan, M. Abdelsalam, Heat transfer correlations for natural convection boiling, Int. J. Heat Mass Transfer 23 (1) (1980) 73–87.
[39] J.G. Collier, J.R. Thome, Convective Boiling and Condensation, third ed., Oxford Science Publications, Oxford, 1994.

[40] R.W. Bowring, A simple but accurate round tube uniform heat flux, dryout correlation over the pressure range 0.7–17 MN/m^2 (100–2500 psia), in: AEEW-R 789.
[41] Y. Katto, H. Ohne, An improved version of the generalized correlation of critical heat flux for convection boiling in uniformly heated vertical tubes, Int. J. Heat Mass Transfer 27 (9) (1984) 1641–1648.
[42] C.N. Ammerman, W.M. You, Enhancing small-channel convective boiling performance using a microporous surface coating, J. Heat Transfer 123 (5) (2001) 976–983.
[43] W. Qu, I. Mudawar, Measurement and correlation of critical heat flux in two-phase micro-channel heat sinks, Int. J. Heat Mass Transfer 47 (2004) 5749–5763.